



OPEN

Hydrodynamics of spike proteins dictate a transport-affinity competition for SARS-CoV-2 and other enveloped viruses

Nicolas Moreno¹, Daniela Moreno-Chaparro¹, Florencio Balboa Usabiaga¹ & Marco Ellero^{1,2,3}

Many viruses, such as SARS-CoV-2 or Influenza, possess envelopes decorated with surface proteins (a.k.a. *spikes*). Depending on the virus type, a large variability is present in the surface-proteins number, morphology and reactivity, which remains generally unexplained. Since viruses' transmissibility depends on features beyond their genetic sequence, new tools are required to discern the effects of spikes functionality, interaction, and morphology. Here, we postulate the relevance of hydrodynamic interactions in the viral infectivity of enveloped viruses and propose micro-rheological characterization as a platform for virus differentiation. To understand how the spikes affect virion mobility and infectivity, we investigate the diffusivity of spike-decorated structures using mesoscopic-hydrodynamic simulations. Furthermore, we explored the interplay between affinity and passive viral transport. Our results revealed that the diffusional mechanism of SARS-CoV-2 is strongly influenced by the size and distribution of its spikes. We propose and validate a universal mechanism to explain the link between optimal virion structure and maximal infectivity for many virus families.

Surface-decorating proteins are ubiquitous in enveloped viruses¹⁻⁷. Depending on the infectious mechanism of the viruses, the surface proteins exhibit characteristic morphology, number, distribution, and reactivity. In general, the infectivity of a virus is greatly determined by the reactivity between receptor-binding domains (RBDs) present on the surface proteins and cell receptors (*affinity*), as well as the available number of binding sites (*avidity*). The coronavirus SARS-CoV-2, responsible for the COVID-19 pandemic, is characterized by an ellipsoidal envelope (E) decorated with protruding functional surface proteins (S), usually referred as *spike* proteins. In the case of SARS-CoV-2, the alignment and binding of the S with the specific angiotensin-converting enzyme-2 (ACE-2) receptor⁸ of the human cells determines the linkage and further insertion of the viral genetic material into the cells. Due to its significance, the structural features of the spikes and their effect on the viral infection process have gained increasing attention to streamlining vaccine development and COVID-19 treatment.

SARS-CoV-2 spikes are formed by three protomers of non-covalently bonded protein subunits⁹⁻¹¹. The binding of the RBD with the epithelium receptor destabilizes the spikes leading to conformational changes in the spike from a tetrahedron-like shape (prefusion) to nail-like (postfusion) morphology¹⁰. Recent evidence showed that this morphological transition of S could also occur before the anchoring to the host cell⁸, and suggested that the ratio between pre/postfusion spikes is a hallmark for novel SARS-CoV-2 variants. Investigations on the inactivated strain of the original SARS-CoV-2 from Wuhan (typically denoted as D-form) revealed spikes dominantly in the postfusion state, around 74 percent¹⁰. In contrast, for mutated variants (also referred to as G-form), only 3% or less were in the postfusion form^{11,12}. Both prefusion and postfusion states appeared randomly distributed on the surface of the envelope. The effect of this morphological transition on the virus infectivity can be significant for vaccine development.

Another distinctive feature of SARS-CoV-2 is a number of spike on the order of $N_s \sim 26 \pm 15$ per virion¹¹, where virion corresponds to the complete infective form of the virus outside the host cell. Compared to other viruses, the N_s of SARS-CoV-2 is close to HIV⁶ (~ 14) and murine hepatitis virus⁷ (~ 11), but significantly lower than other enveloped virus such as SARS-CoV^{1,13} (~ 100), Influenza A⁵ (~ 350), Herpes Simplex⁴ (~ 659), and

¹Basque Center for Applied Mathematics, BCAM. Alameda de Mazarredo 14, Bilbao 48009, Spain. ²KERBASQUE, Basque Foundation for Science, Calle de Maria Diaz de Haro 3, Bilbao 48013, Spain. ³Zienkiewicz Center for Computational Engineering (ZCCE), Swansea University, Bay Campus, Swansea SA1 8EN, UK. ✉email: nmoreno@bcmath.org; mellero@bcmath.org

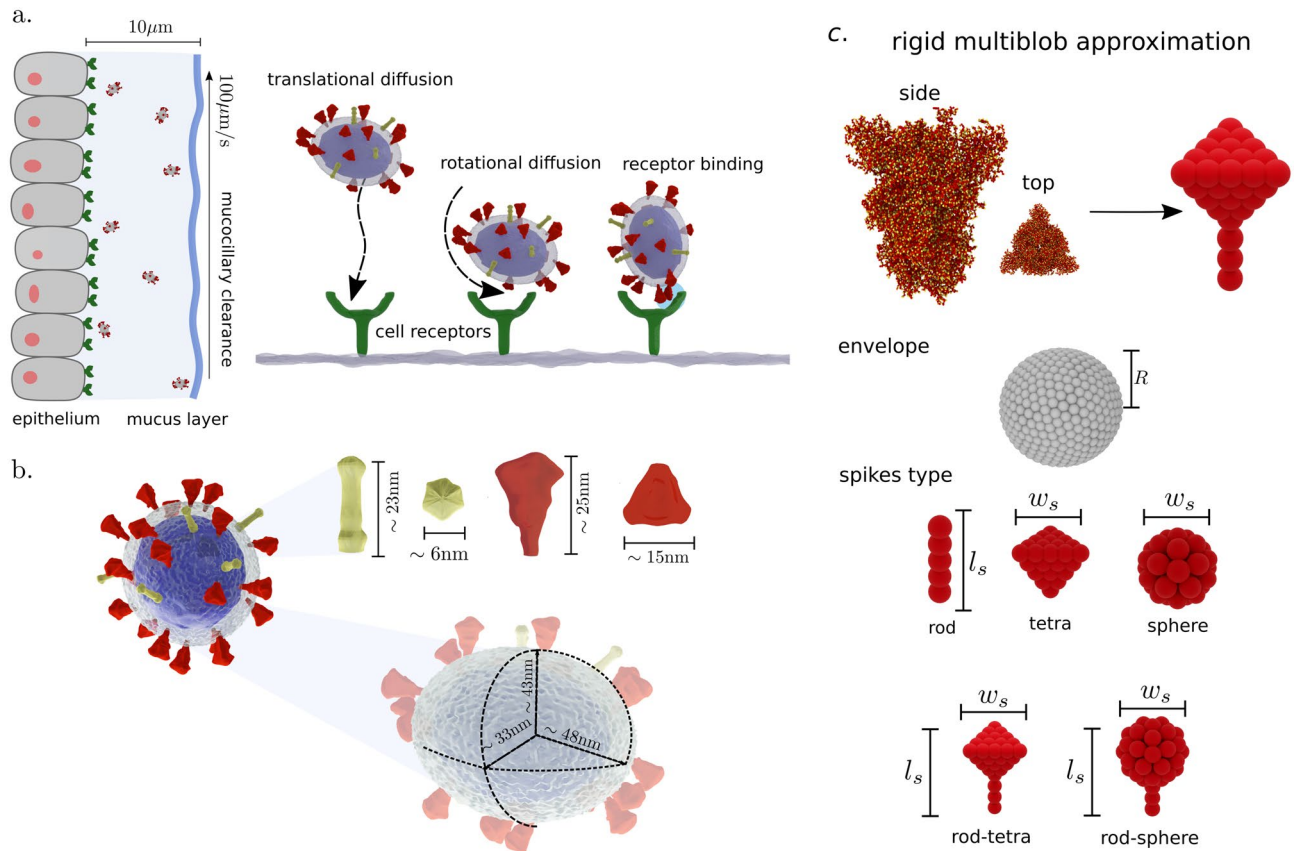


Figure 1. Sketch of viral transport and discretization. **(a)** Representation of viral transport within the first barrier of the respiratory system. Virions diffuse while are advected by the mucociliary clearance mechanism (speed $\sim 100 \mu\text{m/s}$). Effective binding requires translational and rotational diffusion of the virion to the receptor. **(b)** Schematic of SARS-CoV-2 characteristic envelope and spike size. Tetrahedral-shape prefusion S in red and needle-shape postfusion S in yellow. Our envelope and spike discretization for virion diffusion based on the size of the spikes reported experimentally¹¹. **(c)** Hydrodynamic interactions on the scale of the S size are accounted by the model while high frequency atomic motions, fast compared with the virion diffusion, are neglected. Five types of surface proteins morphology are considered: rod, tetra, sphere, rod-tetra, and rod-sphere. Rod, tetra, and sphere are characterized by a single length, whereas rod-tetra and rod-sphere require two parameters.

Lassa² (~ 273), to name a few. Supplementary Table 9, Sect. 8 has a summary of size and N_s for various common viruses. Considering these differences in N_s , an intriguing question is the reason that led the evolution of SARS-CoV-2 towards low N_s and the corresponding effect on virus infectivity. A possible explanation of this disparity is the difference in S reactivity towards receptors and antibodies. In principle, from an evolutionary standpoint, a large N_s would favour cell entry and viral propagation. However, this can also lead to an increased vulnerability of the virus as more S proteins (epitopes) can be targeted by the immune system¹⁴. Another justification lay behind the architecture constraints on the maximum N_s a viral envelope can display. Evidence in other coronaviruses¹³ has shown that N_s correlates with the size E and the flexibility of the constituting membrane proteins. Overall, the reason behind the variability in N_s between enveloped virus and the characteristic lower number for SARS-CoV-2 is yet to be identified. Herein, stemming from a fluid dynamics standpoint, we postulate that spikes morphology, number, and distribution have a crucial effect on virus mobility, which determines the balance between reactivity and transport in ways to promote viral infectivity.

When studying the infectivity mechanism, it is also essential to consider the transport of the virion to the epithelium, where the linkage takes place. The first barrier in the human body against viral infections is the mucus, which covers the surfaces of the respiratory, reproductive, and gastrointestinal tracts^{15,16}. In the mucus, the glycoproteins mucins trap the pathogens forming a gel network with pore size ranging from 200–500nm¹⁷. However, it has been shown that with such pore size, small virions can diffuse unhindered through the mucus¹⁵ unless the virion form affinity bonds with the mucins. In the respiratory tract, the mucus layer has a thickness from 1 – 10 μm ¹⁸, and transports the immobilized pathogens to the pharynx for neutralization (see Fig. 1a). For SARS-CoV-2, the virion needs to cross that barrier to reach the epithelium before the clearance. As the virions are not self-motile, their motion relies on the advection of the transporting fluid, as well as the diffusion of the virion in the media (see Fig. 1a). In general, the diffusive transport set the upper bound on the time scale at which virions can interact with the host cell.

	water		blood		nasal mucus	
Virion	D_t [$\mu\text{m}^2/\text{s}$]	D_r [1/s]	D_t [$\mu\text{m}^2/\text{s}$]	D_r [1/s]	D_t [$\mu\text{m}^2/\text{s}$]	D_r [1/s]
SARS-CoV-2 (G-form)	4.0	965.5	1.2	275.9	$2.5 \cdot 10^{-3}$	0.6
SARS-CoV-2 (D-form)	4.3	1185.3	1.2	338.6	$2.7 \cdot 10^{-3}$	0.7

Table 1. Translational and rotational diffusivities computed for different virions in water, blood, and nasal mucus. The diffusivities of the virions are computed using Eq. (5) in “Methods” section. The viscosity η values are for water = 0.001 Pa · s, blood = 0.0035 Pa · s²⁴ and, nasal mucus = 1.6 Pa · s¹⁶. Temperature = 298.15 K, and $k_b = 1.38064852 \cdot 10^{-23} \text{ m}^2\text{kg/s}^2\text{K}$.

The SARS-CoV-2 virion can be described as a nanosized ellipsoid with radius of their principal axes $R_1 \sim 48 \text{ nm}$, $R_2 \sim 43 \text{ nm}$, and $R_3 \sim 33 \text{ nm}$ ¹¹ (see Fig. 1b). From the Stokes-Einstein theory, the translational and rotational diffusion arises from the hydrodynamic interactions and depend on the morphological features of the virion and the viscosity of the fluid. Mobility predictions using the Stokes-Einstein theory have shown to be in good agreement with the transport of aquatic viruses¹⁹. At the nanoscale, the rotational diffusion of such decorated objects may exhibit characteristic deviations compared to a homologous not-functionalized ellipsoid. Furthermore, since the shape and distribution of **S** can alter its diffusion rate, a detailed characterization of the virions diffusivity may provide rheological signatures to differentiate various virus types, as shown in the pioneering work by Kanso and coauthors^{20,21} using rigid bead-rod theory.

Here, we adopt the rigid multiblob methodology²² (RMB) (see “Method” section and Sect. 1. SI) to investigate the mobility of virion models computationally. Using the recently reported structure of SARS-CoV-2¹¹, we consider the effects of spikes distribution and morphology on the complex diffusive transport of the virus suspended in a single fluid. Using the RMB, we construct precise mesoscale models that allow us to incorporate consistently thermal fluctuation effects and hydrodynamic interactions with the suspending media. In these models, we neglect **S** mobility on the envelope surface and the envelope deformability. This simplification allows us to construct tractable models to investigate over whole-virion diffusional time scales. In general, for unbounded virions we expect deformability to have weak influence on their mobility. However, this effect may become relevant for virions moving towards cellular walls during the viral entry. The proposed approximation allows us to elucidate the morphological features that affect the hydrodynamic behaviour of the SARS-CoV-2 and offer potential applications as rheological biomarkers. Moreover, we show that the hydrodynamic characterization elucidates a universal mobility mechanism among different families of enveloped viruses.

Results

Virion diffusion. Using the RMB we discretize the virion as a set of rigidly connected blobs (see Fig. 1c), and consider that it moves as a rigid object. We construct virion models with spherical and ellipsoidal **E** of size R , and investigate the effects of **S** shape on mobility using five different morphologies inspired by surface proteins reported in the literature for various viruses (i.e. HIV, MVH, Denge, SARS-CoV, Lassa, Herpes, Influenza). We adopt the following labelling for the investigated shapes: *rod*, *sphere*, *tetra*, *rod-sphere*, and *rod-tetra*. Rod, tetra, and sphere shapes possess only one characteristic size: length (l_s/R) or width (w_s/R), whereas for rod-tetra and rod-sphere both l_s/R and w_s/R are defined (see SI Sect. 8). To account for **S** distribution on the surface of **E**, we construct virions with both homogeneous and randomly localized **S**. Following the SARS-CoV-2 morphology reported by Yao et al.¹¹ (based on cryo-ET and subtomogram averaging), we construct SARS-CoV-2 models using an ellipsoidal **E**, with rod-tetra (prefusion) and rod (postfusion) **S**, localized in random configurations. Since nearly spherical **E** have been also reported¹² for SARS-CoV-2, we discuss possible effects of **E** morphology in the following section.

Based on the currently known structures¹¹ of SARS-CoV-2 in their original (D-form) and mutated (G-form) strains, we give, in Table 1, a breakdown of the numerically-estimated diffusion coefficients for three different media viscosities: water, blood, and mucus (see Supplementary Table 12 a full list of D_t and D_r for other virions). Strictly speaking, the diffusion of the virion in complex fluids is strongly determined by microrheological features such as mesh size (mucus) or the presence of other constituents on the length scales of the virion. Given the size of SARS-CoV-2 ($\sim 90 \text{ nm}$), we expect it to diffuse nearly unhindered on typical mucus meshes (200–500 nm). However, we also provide the estimated diffusion coefficients using the macroscopic viscosities of blood and mucus as an upper-bound indicative for the virion diffusivity. Diffusion coefficients in crowded biological environments have been reported to decrease over 1000-fold, compared to diffusion in water²³. For comparison, in Supplementary Tables 4 and 5, we compiled the estimated diffusivities of SARS-CoV-2 on the range of the variance on number of spikes reported.

In the remaining, to streamline the discussion, we introduce a reduced translational $\bar{D}_t = D_t|_{\text{virion}}/D_t|_{\text{envelope}}$ and rotational $\bar{D}_r = D_r|_{\text{virion}}/D_r|_{\text{envelope}}$ diffusion coefficients. Where $D|_{\text{envelope}}$ is the calculated diffusivity for an envelope without **S**. Reduced diffusivities allow us to rationalize the results in terms of **S** count and morphology. The results described herein correspond to resolutions with discretization errors below 3%. while convergence results are presented in the Sect. 4 of the supporting information (Supplementary Tables 1–5 summarize the convergence errors for the **E** optimal **E** resolution, resolution convergence for the whole SARS-CoV-2 virion **E** and **S** and convergence errors for tetrahedral **S** respectively).

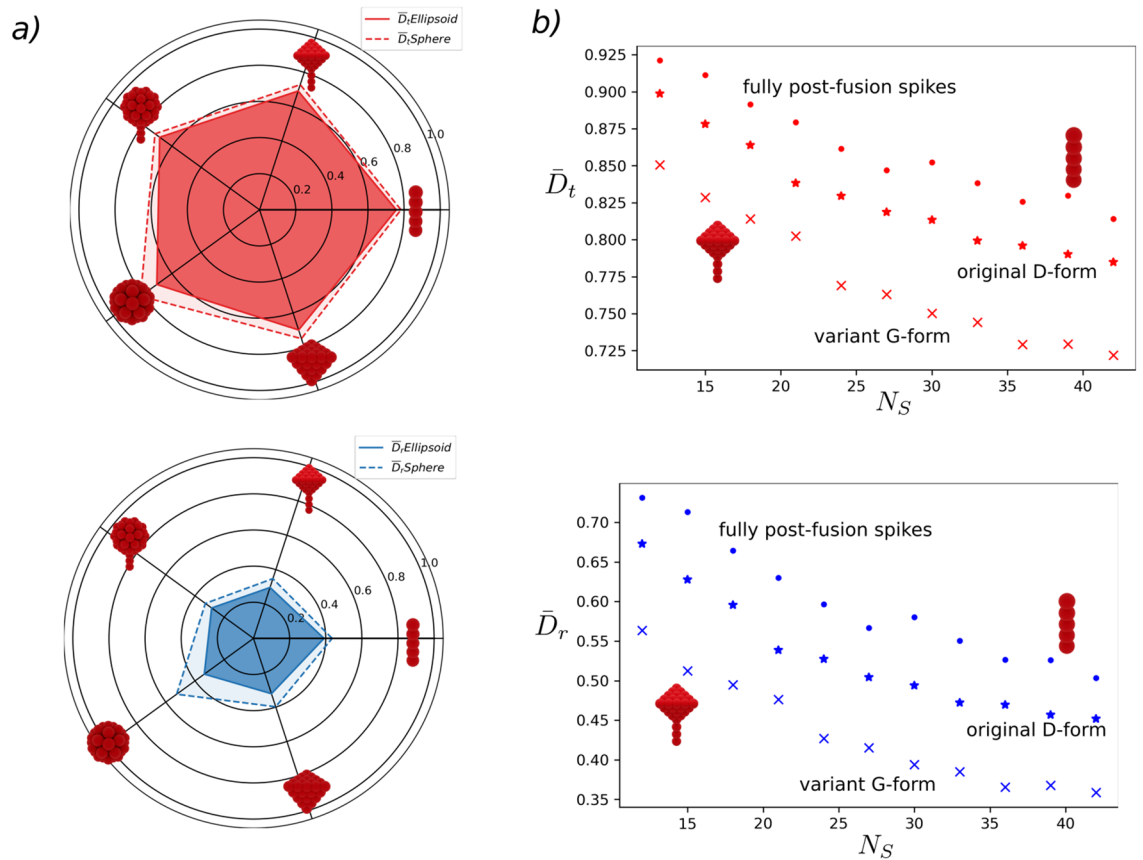


Figure 2. Effect of **S** morphology on the mobility of virions. **(a)** Comparison of the reduced translational and rotational diffusion for the different **S** shapes for virions with $N_s = 12$, and $l_s/R = 0.4$, homogeneously distributed. Ellipsoidal envelopes exhibit slightly larger deviations on the rotational diffusion than spherical envelopes due to their small asymmetry. The differences in \bar{D}_t between **S** shapes do not reveal a significant difference. In contrast, for \bar{D}_r , small but observable differences indicate the potential use of the rotational diffusion of virions as a rheological biomarker. **(b)** Variation on \bar{D}_t and \bar{D}_r with N_s for fully postfusion (rod), fully prefusion (rod-tetra) and mixed postfusion/prefusion **S**. The diffusion coefficient values for each N_s are obtained from ten independent realizations with **S** randomly distributed on the envelope. The fraction of postfusion **S** in the mixed case corresponds to the original D-forms of SARS-CoV-2, $N_{s|post}/N_s = 0.7$. Fully prefusion case is consistent with mutated G-forms characterized by $N_{s|pre}/N_s \sim 1$. Regardless of the differences in **S** morphology, the reduction in both \bar{D}_t and \bar{D}_r exhibits the same functional dependence as N_s increases. However, the magnitude of the mobility reduction is larger for the full-prefusion case.

Envelope shape and surface proteins distribution. In general, axial asymmetry of **E** can favour directional motion of the virions¹⁸. However, for SARS-CoV-2 **E** we observed weak effect of envelope shape on virion mobility, only on the order of 1% for \bar{D}_t and 2% for \bar{D}_r (see 2a). The later, may indicate that the dominant effect of ellipsoidal shapes is to maximize the available surface area for the proteins in **E**, whereas keeping virion transport unaffected. In contrast, the distribution of **S** showed to have a more important role on virion transport. For all the surface proteins investigated we found a relative increment on both \bar{D}_t and \bar{D}_r , when **S** are localized at random positions around the surface relative to the homogeneous case (see SI Sect. 6 Supplementary Fig. 3 and Supplementary Table 8). In particular, for rod-tetra type (used for SARS-CoV-2), the increment on \bar{D}_r ranged from 10% to 3%. We speculate that the sparsity and randomness of **S** favour the ability of the virion to explore its surroundings to reach binding receptors. This is consistent with all-atoms simulations²⁵ of **S**, which suggested that the conformational freedom of the spikes in **E** may increase the infectivity of the virus by providing mechanical robustness, facilitating motions to avoid antibodies access, and increasing the avidity when binding the cell²⁵.

Surface proteins shape and size. In Fig. 2a, we compare the reduced translation and rotational diffusivity for the five types of **S** studied for virions with 12 homogeneously distributed **S** and fixed size, for both spherical and ellipsoidal envelopes. The presence of **S** induces a reduction in the translational diffusion of the virions between 20 to 30 per cent (compared to the naked envelope), whereas the impact in rotational diffusion is more significant, ranging from 50 to 70 per cent. Significantly, the shape of **S** determines the extent of the reduction on both \bar{D}_t and \bar{D}_r . Overall, larger surface proteins affect the transport properties of the virion strongly. The small but noticeable differences in the diffusion between globular and tetrahedral **S** indicate a characteristic transport

Virus					ΔD_t		ΔD_r	
	N_s	l_s/R	w_s/R	$V_s/R^3 \cdot 10^{-3}$	N_s^∞	b	N_s^∞	b
MHV ⁷	11	0.47	0.24	20.46	158	24	171	15
HIV ⁶	14	0.20	0.25	9.81	110	16	145	11
SARS-CoV-2 ¹¹	26	0.52	0.31	39.95	205	9	207	5
Dengue ³	60	0.55	0.20	17.28	229	15	197	9
SARS-CoV ¹	83	0.32	0.36	32.57	169	18	211	12
Lassa ²	273	0.14	0.15	2.46	374	53	373	41
Influenza ⁵	350	0.25	0.12	2.67	579	70	581	54
Herpes Simplex ⁴	659	0.22	0.05	0.48	753	116	844	94

Table 2. Summary of characteristic N_s , l_s , w_s , and surface protein volume V_s/R^3 for different virions, along with the fitted parameters N_s^∞ (± 2) and b (± 2 for ΔD_t and ± 3 for ΔD_r) from (1). All the parameters obtained from fitting of (1) lead to a determination coefficient $R_d^2 = 0.99$.

signature that can be further exploited for virus identification. In SI Sect. 13 (Supplementary Figs. 15 and 16), we show the relative differences in mobility for the S shapes evaluated.

Regarding the effect of the S size (l_s/R and/or w_s/R) we found, as expected, that larger proteins considerably reduce the diffusion of the virions in all cases. Nevertheless, the dimensionality of the S affects the scaling of diffusion with the S size. For instance, comparing rod- and tetra-type shapes, rod shapes (that are dominantly one dimensional) showed a weaker variation on \bar{D}_t and \bar{D}_r as the size increases (see Supplementary Fig. 4). In contrast, tetra-shape S displayed a strong reduction on diffusivity (see Supplementary Fig. 5). Overall, we observed that the virions with bulkier and larger surface proteins (compared to the envelope size) had an intrinsic diffusional penalty. Therefore, the regulation on the number of S suggests a possible alternative to compensate for this reduction in mobility.

Number of surface proteins. Now, we switch attention to the role of the number of surface proteins on the mobility of the virion. In Fig. 2b, we compile the variation on translational and rotational diffusion for virions with different rod and rod-tetra S shape. Overall, leading to reductions ranging from 10 to 30 percent in the \bar{D}_t and 30 to 70 percent in \bar{D}_r , as the N_s increases. Interestingly, the dependency of \bar{D}_t and \bar{D}_r with the N_s decays in the same fashion, regardless of S type. In Fig. 2b the range N_s presented corresponds to the experimentally reported^{11,12} for SARS-CoV-2 virions with fully-postfusion S (rod), fully-prefusion S (rod-tetra), and mixed S. The later is consistent with the original Wuhan strain, or D-form. Whereas fully-prefusion resembles mutated strains, G-form. In general, the larger population of S in prefusion states in mutated variants induces a reduction in the mobility of the virion, and this decay occurs quickly after a few number of spikes are added on the surface of E. Interestingly, the mobility appears to reach a saturation condition where the diffusion rate of the virions is modestly affected by the increase in N_s . In general, a lower bound in the diffusion is expected as N_s increases reaching a closed packing situation on the E surface. Thus, the occurrence of a saturation condition is consistent with the rate at which the lower bound is attained. Asymptotic saturation conditions for both transport and reactions have been reported for ligand-receptor interactions using functionalized colloids²⁶ and other viruses such as HIV¹⁴.

To explore further the decay in mobility due to N_s , we modelled various enveloped viruses (Fig. 3a) using the characteristic sizes reported in the literature (in Supplementary Table 10 we compile N_s , size, and S shape for de different virions, and in Tables 11, 12 the estimated reduced diffusivities). Remarkably, we identified that the form of the decay in \bar{D}_t and \bar{D}_r (see Supplementary Figs. 6 and 7) is consistent in other viruses, as shown for \bar{D}_r in Fig. 3a. However, the magnitude of the drop in mobility depends on the S shape and size. For example, Herpes virions with $l_s/R = 0.22$ can exhibit upto 23% drop in \bar{D}_r , whereas SARS-CoV-2 with $l_s/R = 0.52$ showed reduction up to 70%.

Considering that the diffusivity of the virions varies between one corresponding to an envelope without S ($\bar{D}_i = 1$) and one with closely packed S ($\bar{D}_i = \bar{D}_i^\infty$) we introduce the *excess* diffusion coefficients $\Delta D_i = (\bar{D}_i - \bar{D}_i^\infty)/(1 - \bar{D}_i^\infty)$, for $i = t, r$. This expression varies from 1 when $N_s = 0$ to 0 when $N_s = N_s^\infty$. The term N_s^∞ is the number of S at which the virion mobility saturates, \bar{D}_i^∞ , and the effect of N_s is negligible. Based on the computed translational and rotational diffusivities we postulate the following expression to describe the excess diffusion dependency with N_s

$$\Delta D_i = \frac{\bar{D}_i - \bar{D}_i^\infty}{1 - \bar{D}_i^\infty} = \begin{cases} \frac{N_s^\infty - N_s}{N_s^\infty} \left[1 - e^{-\frac{b}{N_s}} \right], & \text{for } N_s \leq N_s^\infty \\ 0, & \text{for } N_s > N_s^\infty \end{cases} \quad (1)$$

where N_s^∞ and b are fitting parameters that depend on the characteristic size of the S. The first term on the right-hand side of (1) accounts for a linear dependency on N_s before reaching \bar{D}_i^∞ . Similar linear dependence on N_s has been identified for ligand-receptor interactions using functionalized colloids²⁶. The second term on the right-hand side of (1) describes an exponential decay in the diffusivity that is controlled by the shape-dependent parameter, b . Using the calculated \bar{D}_i and taking \bar{D}_i^∞ from the largest N_s simulated, equation (1) allows us to obtain the characteristic values of N_s^∞ and b , for various families of enveloped virions as presented in Table 2

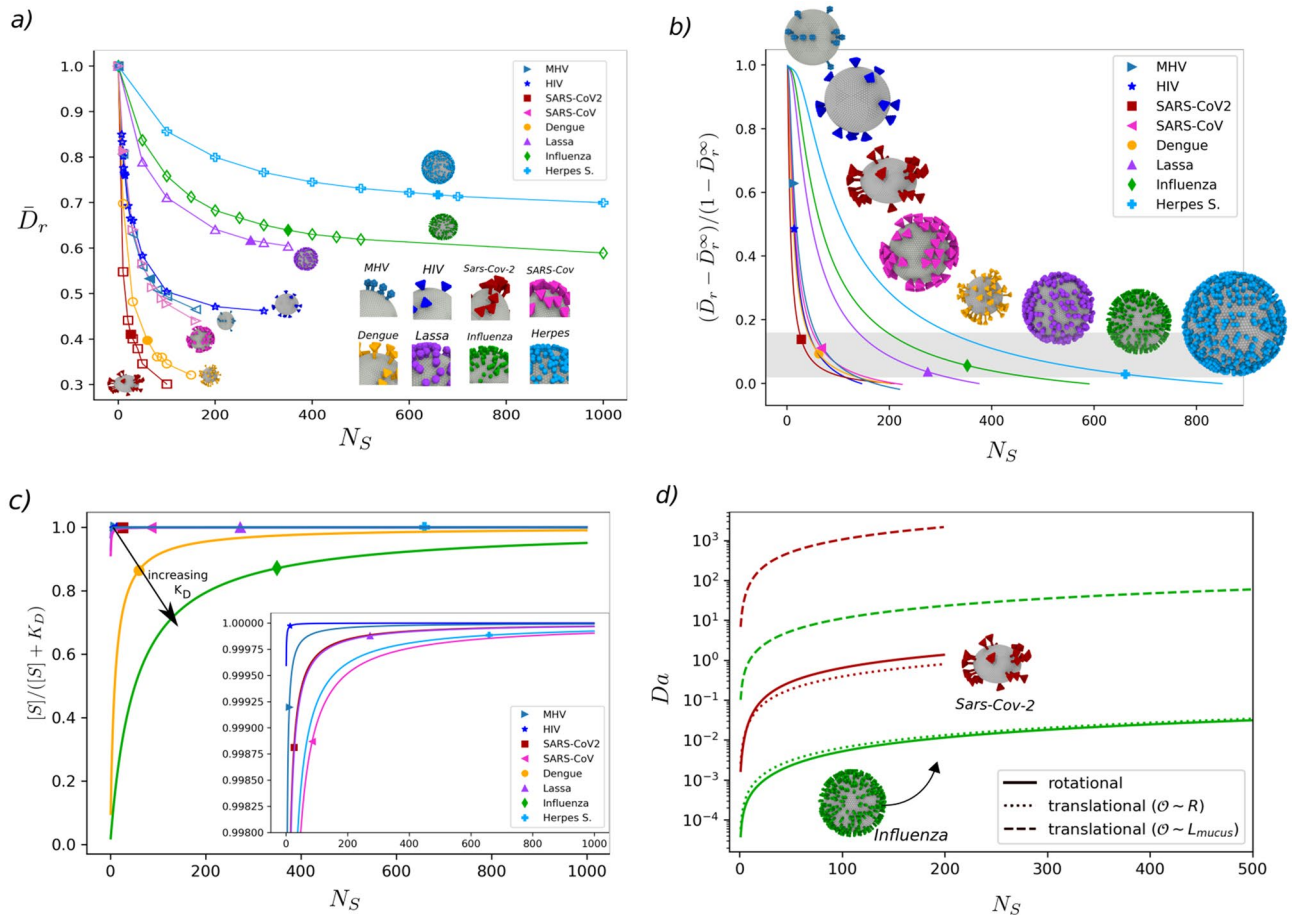


Figure 3. Interplay between virion rotational diffusion and receptor binding affinity for SARS-CoV-2 and selected viruses. **(a)** Effect of N_s on the rotational diffusion. Each virion family exhibits a characteristic reduction on its mobility reaching an asymptotic value for large N_s . The maximum N_s evaluated for the different viruses correspond to the condition where surface proteins overlap. SARS-CoV-2 shows the sharpest drop in diffusion, whereas for Herpes Simplex the reduction occurs over a much larger N_s range. Inset: Snapshots of the morphologies used to represent each virion type. In the Methods Section we include the reported crystal structure and sizes of the surface proteins for comparison. **(b)** Dependence of the excess rotational diffusion with N_s (fitted from Eq. (1)) for different viruses. Filled markers indicate the experimentally reported N_s for the different viruses. For the majority of viruses modelled the mean values of the excess diffusion (translational and rotational) are $\Delta D_t \sim 0.08$ and $\Delta D_r \sim 0.12$, elucidating a characteristic trend in their mobility state regardless of the type of virus and N_s . This suggests the existence of a general transport mechanism across enveloped viruses. This ground state is likely induced as a balance between their geometrical features and S reactivity. The higher ΔD_r in HIV and MHV can be explained due to an enhanced mobility of S on the E surface. Such effect is not currently accounted in our model. The fitting parameters obtained from fitted from Eq. (1) are summarized in Table 2 and SI Sect. 9. **(c)** Saturation function change with N_s for various virus based on their binding constant K_D to cellular receptors. The magnitudes of K_D are summarized in Supplementary Table 14. The majority of the viruses passes a high saturation value (~ 1) over the range of N_s reported. Influenza A and Dengue show the lowest level of saturation. This lower saturation for Influenza A viruses may explain its characteristic variety of pleiomorphic structures⁵ as a way to enhance infectivity. Inset plot: Zoom over the saturation levels of SARS-CoV-2, HIV, Herpes and Lassa virions. HIV reaches saturation at very low N_s . **(d)** Translational and Rotational Damkohler number change with N_s for SARS-CoV-2 and Influenza A virus. At the length scales of the E size R , the reaction time for Influenza viruses is kinetically controlled due to its low affinity, whereas for SARS-CoV-2 the rotational and kinetic time scales are on the same order. When accounting for the whole binding process, the translational diffusion on the length scales a mucus layer with thickness of $L_{mucus} = 5 \mu\text{m}$ amounts for the larger part of the required time.

and SI (Supplementary Fig. 8 and Supplementary Table 13 Sect. 9). In Fig. 3b, we depict the variation in ΔD_r for different viruses along with the experimentally reported N_s . The maximum N_s evaluated for each virion is determined as limiting condition where S overlap. Except for HIV and MHV (with $\Delta D_r \sim 0.5$), independently of the type, we identify a characteristic trend in the mobility, with a mean $\Delta D_t \sim 0.12$ and $\Delta D_r \sim 0.08$ among all the viruses. This suggests the existence of a general transport mechanism across enveloped viruses. We speculate that this mobility regime coincides with condition where reactivity and mobility balance out. For each

type of virion, the shape and size of **S** determines hydrodynamically how much the mobility can change, while the reactivity of **S** sets the extent of such reduction in \bar{D}_t and \bar{D}_r . Thus, this interplay is conserved across virus families. In the following section we address this hypothesis. The differences found for HIV and MHV may be associated with a higher mobility of the surface proteins or specific interactions with the surrounding mucus, that are not accounted in the current model.

Affinity-Mobility balance. As the viral spikes of SARS-CoV-2 mutate into new variants with potentially different affinities but equivalent spikes size, it is necessary to elucidate the relative balance between affinity and mobility. To consider only affinity effects, it is customary to determine the strength of the spike-receptor interactions measuring the binding affinity constant, K_D ²⁷. For a given K_D and concentration of **S** [S] surrounding the envelope, it is possible to introduce a saturation function $[S]/([S] + K_D)$ that relates the affinity with N_s . The **S** concentration [S] variation with N_s is approximated using the volume around the envelope. This volume is given by the radius of the envelope and the height of the **S** (see SI Sect. 10). The saturation function varies from 0 ($[S] \ll K_D$) when the concentration of **S** is a limiting factor for binding to occur, to 1 ($[S] \gg K_D$) when **S** availability is ensured facilitating binding. In Fig. 3c, we present the variation of the saturation function for G-forms of SARS-CoV-2, along with another viruses for comparison (see Supplementary Table 14 for the K_D values of the viruses and receptors). For SARS-CoV-2 HIV, Lassa, and Herpes, we find that the saturation function reaches values close to unity for a small number of spikes. In contrast, Influenza A exhibits the lowest saturation, even at significant N_s . In general, after comparing the experimentally measured N_s , the effect of K_D alone is not sufficient to rationalize the difference in N_s among the investigated virions.

Since the effective reaction time t_r for virion/receptor association would depend on diffusional t_d and binding t_b time scales, we use the non-dimensional Damkohler number $Da = t_d/t_b$, to identify the controlling mechanism virion/receptor association. The diffusional time $t_d = t_t + t_r$ accounts for both translation and rotation leading to the definition of both Da_t and Da_r . In general, t_b controls the reaction rate for low-affinity interactions, whereas t_d determine reaction rate for interactions requiring the alignment or localization of the ligand/receptor pair²⁸. Theoretical models on ligand-receptor interactions mediated by rotational diffusion²⁶ showed that t_r is linear function of the N_s and the relative surface occupied by **S**²⁶. Here, we estimate t_b using the reported association reaction constant K_{on} between **S** and ACE-2^{8,29}, for the original D-form ($K_{on} = 1.37 \cdot 10^5$ [Ms]⁻¹) and mutated G-form ($K_{on} = 7.92 \cdot 10^4$ [Ms]⁻¹) SARS-CoV-2 strains. For SARS-CoV-2, we obtain $Da_t \sim 0.4$ and $Da_r \sim 0.2$ for the D- and G-forms, respectively. Similar order of magnitude is observed for Da_t for diffusion on the length scales of the virion size. These values of $Da \sim 1$ evidence that SARS-CoV-2 and its variants are effectively on a regime where both affinities and mobilities are highly coupled. This value is in contrast with the affinity-controlled regime of Influenza A that exhibit the lowest affinity among the virus investigated (see SI Table 14) with $K_{on} = 700$ [Ms]⁻¹¹⁸, leading to $Da_r \sim 1 \cdot 10^{-2}$. In Fig. 3d, we present the variation of Da_t and Da_r for different spikes number for SARS-CoV-2 and Influenza A, for comparison. For the first entry, considering that the virion crosses a mucus barrier of $\approx 5\mu\text{m}$ the maximum diffusional time t_d^∞ is determined by \bar{D}_t over the length scale of the mucus thickness. Thus leading an overall binding process dominated by transport $Da > 1$. In SI Sect. 12 (Supplementary Figs. 12–14), we have summarized translational and rotational time scales for the different virion types, for the first entry stage.

If we consider that the energy of binding between RBDs and a cell receptor is $\varepsilon_{\text{bind}}$, the strength of all the interactions combined (upto a first order approximation) can be expressed as $\Gamma = N_s \varepsilon_{\text{bind}}$. In general, increasing N_s should favor virion avidity, whereas reducing the diffusion rate of the virion as shown in Fig. 3b. For convenience, we introduce a geometrically constraint avidity $\bar{\Gamma}$, given by

$$\bar{\Gamma} = (\Gamma/\Gamma^\infty)^\alpha, \quad (2)$$

such that $0 \leq \bar{\Gamma} \leq 1$, independently of the value of $\varepsilon_{\text{bind}}$. The exponent α in (2) incorporates non-linearities in the binding between RBDs and a cell receptors. For linearly dependent interactions we have that $\alpha = 1$. The limit $\bar{\Gamma} = 1$ indicates the saturation condition, where the increase in N_s no longer influences the binding. The magnitude of $\Gamma^\infty = N_s^\infty \varepsilon_{\text{bind}}$ depends on the characteristic envelope size R and **S** volume. The use of N_s^∞ to determine the behavior of $\bar{\Gamma}$ assumes that both mobility and reactivity saturate on the same order of N_s , however, this may change as the order of reaction between **S** and receptors changes.

Now, we define an infectivity parameter $\mathcal{I} = \Delta D_r \bar{\Gamma}$ that considers the interplay between the transport and reactivity. On one hand, independently of the strength of the interactions between the virions and the epithelium, the time required for the virion to reach available anchoring sites is inversely proportional to the diffusivity of the virus. On the other hand, regardless of the time taken to the virion to reach the receptors, a successful binding depends on the avidity of sites. The parameter \mathcal{I} accounts for the transport limiting condition through ΔD_r , and the reaction limiting condition through $\bar{\Gamma}$. In Fig. 4, we present the variation of \mathcal{I} with N_s for SARS-CoV-2. Remarkably, the maximum in \mathcal{I} that balance avidity and mobility coincides with the reported values for spikes count for SARS-CoV-2¹¹ (26 ± 15). Similarly, the maximum in the infectivity curve for other virion models SARS-Cov, Lassa, Denge, Herpes Simplex, and Influenza A is in close agreement with experimental evidence^{1–5}. We must highlight that the proposed infectivity parameter, \mathcal{I} , describes the balance between transport and affinity, indicating an optimal condition for each virus family. However, it does not provide the absolute value of the virus infectivity, which indicates the spreading effectivity of the virus. Determination of the actual spreading rate requires the complementary knowledge on the infection process over disparate spatio-temporal scales (extracellular transport, binding, and endocytosis), likely involving various computational methods. In Fig. 4 we use a corrected exponent α that depends on the available area of **S**. The corrected exponent is given by $\alpha = 1 + b/100$, where b is the shape-dependent parameter obtained from (1). We remark that HIV⁶ and MHV⁷ showed a small deviation from the maximum \mathcal{I} . The differentiating behavior for HIV, can be related with the presence of highly

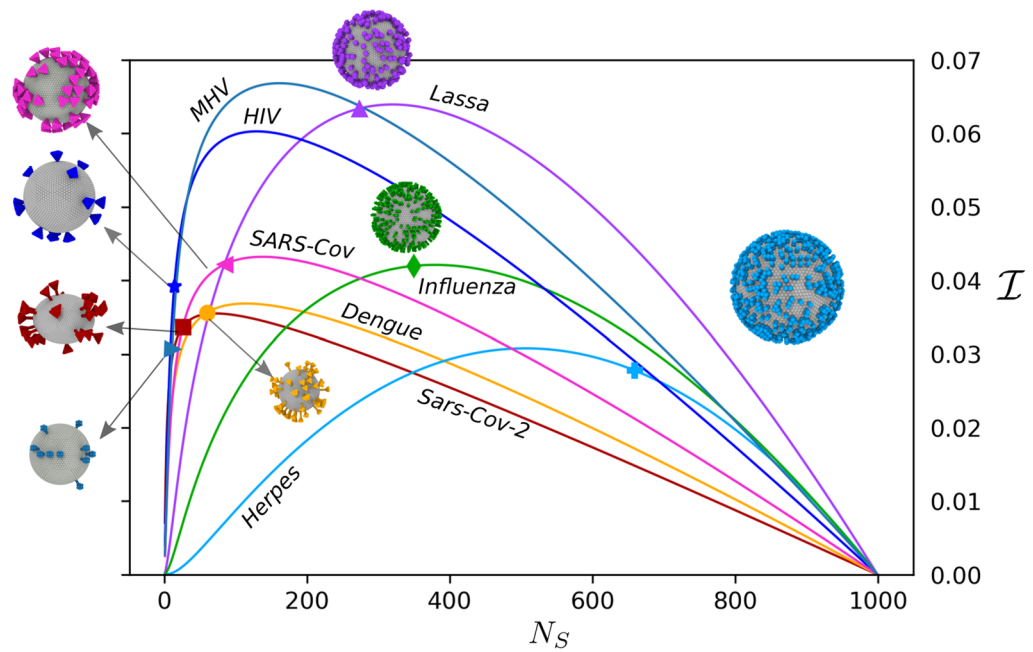


Figure 4. Interplay between virion rotational diffusion and receptor binding affinity for SARS-CoV-2 and selected viruses. The figure shows the variation in the infectivity parameter \mathcal{I} with the number of surface proteins. The markers indicate the experimentally reported values of N_s for each virion type, which in most cases matches well with the theoretical optimum value. HIV and MHV are two exception with particular low values of N_s , perhaps related with enhanced mobility of **S** around the envelope, specific virus/mucus interactions, or an earlier reactive saturation requiring fewer **S** than N_s^∞ due to strong binding affinities with their receptors.

reactive **S** able to reach early avidity saturation, Γ^∞ , or the ability of **S** to diffuse on the **E** surface³⁰. These effects are not accounted in our current model, however, they will be addressed in future publications. As the viruses reach optimal conditions the sensitivity \mathcal{I} may reach a limit where comparing virus variants is challenging. Additional information regarding the surface proteins affinity combined with geometrical features may shed light on this evolutive refinement. On the direction of the morphological changes driven by reactivity, a recent study³¹ proposed that antibody pressure can be responsible for the evolution of surface proteins. In this situation morphological changes occur on atomistic scales, that would be typically hindered in our model.

Discussion

The emergence of novel SARS-CoV-2 variants poses a significant challenge. Important information is known regarding the location and effect of the existent mutations^{27,29}, providing relevant insights. However, the transmissibility of viruses within and among hosts may exhibit features that go beyond the particular genetic sequence¹⁸. In this context, morphological features can be studied to reveal similarities and differences between different virus families. The current results provide an initial step for further microrheological characterization of viral solutions that can serve as a tool to identify potential biomarkers and overall gaining an understanding of viral functionality.

We show how the interplay between surface-proteins distribution, shape, size affect the mobility of the virions. We postulate that transport properties of the virions roots from geometrical constraints that can explain the differences in **S** density across a variety of virus. Thus, these geometrical constraints, along with the affinity of the RBD of the proteins, may indicate how different virus families exist on optimal evolutionary conditions. The saturation values on **S** affinity and along with \mathcal{I} , justify the lower N_s reported for SARS-CoV-2 and its variants. From an evolutionary standpoint, SARS-CoV-2 may have reached an optimal avidity/mobility balance that ensures a large mobility due to a moderate value of N_s and a large affinity to the receptors groups thanks to a high saturation value. Experimental validation of the proposed infectivity curve requires a more systematic investigations able to control the number/size of envelope proteins in the viruses. On this direction, experimental techniques using pseudo viruses (viral envelopes functionalized with different surface proteins) along with single virus tracking techniques^{32,33} offer a good route for validation. Another *in-vitro* setting with potential for validations is the use of magnetorheology. In this case, viruses can be functionalized using magnetic nanoparticles³⁴. The rheological response of the virus can be then correlated to the rotational and translational diffusion of the virions.

The understanding of the virus spreading through the first barriers of defense in our body is in general difficult, the complexity and nonlinearity of the interactions between the media and viruses makes difficult the investigations using experiments alone. Our results offer a good approximation of virion transport properties based on physiological conditions that can be further used in viral modelling. Additionally, in a more general sense can potentially guide the design of vectors for nasal vaccines that optimize immune response³⁵. Our

findings also provide tools for the designing of microrheological devices for screening, detection, and characterization of viruses.

Methods

Virion diffusivity. At low Reynolds number the deterministic motion of the virion can be approximated in terms of the Stokes equations, such that

$$\mathcal{U} = \mathbf{M}\mathcal{F}, \quad (3)$$

where $\mathcal{U} = \{\mathbf{u}, \boldsymbol{\omega}\}$ is the vector of the linear (\mathbf{u}) and angular ($\boldsymbol{\omega}$) velocities, $\mathcal{F} = \{\mathbf{f}, \boldsymbol{\tau}\}$ is the vector formed by the total forces (\mathbf{f}) and torques ($\boldsymbol{\tau}$) exerted on the body. The tensor \mathbf{M} has denoted the mobility and depends only on the shape of the body. This tensor provides information about the hydrodynamic interactions acting on the body. Here, we determine mobility \mathbf{M} by solving the Stokes equations with the rigid multiblob method²² (see SI Sect. 1. for a detailed description). The virions envelope and surface proteins are discretized as a set of rigidly-connected blobs of size r_b , located at a distance $r_o = 2r_b$ between blob centers. Depending on the size of the modelled object, R_{object} , and the distance between blobs, r_o , we define the resolution as R_{object}/r_o . In Supplementary Figs. 1 and 2 we illustrate the characteristic discretization dimensions of **E** and **S** respectively. In Sect. 11 of SI we describe the construction of discrete morphologies for **E** (Supplementary Fig. 9) and **S** (Supplementary Figs. 10 and 11). We use resolutions fine enough to compute the mobilities with errors below 3%, see SI Sect. 4 for convergence results.

The translational³⁶ and rotational³⁷ diffusivity of can be then computed using the numerical approximation of \mathbf{M} , as

$$D_t = \frac{k_B T}{3} \text{Tr}(\mathbf{M}_t), \quad (4)$$

$$D_r = \frac{k_B T}{3} \text{Tr}(\mathbf{M}_r), \quad (5)$$

Where k_B is the Boltzmann constant, T is the temperature. The tensors \mathbf{M}_t and \mathbf{M}_r are the translational and rotational components of the mobility. This approximation considers that the virus moves as a rigid object, thus neglecting **S** mobility on the envelope surface. Nevertheless, this approximation allows us to elucidate the morphological features that affect the diffusion of the virions. Such morphological features offer potential applications further to analyze similarities and differences between different virus families.

Data availability

The data that support the findings of this study are available from the corresponding author, upon reasonable request.

Appendix

Envelope shape. Virion shape and size have been reported to affect the efficiency of the virus to penetrate through mucus mesh (the first barrier before accessing endothelial cells in the upper airways). For influenza, for instance, pleiomorphic variations have been speculated to correlate with infectivity and pathogenicity⁵. In the classic cartoon of SARS-CoV-2, it is considered as a spherical envelope surrounded by tightly packed and homogeneously distributed **S**. However, recent investigations using cryoelectron tomography (cryo-ET) and subtomogram averaging (STA) provide us with a realistic picture of the complete three-dimensional description of SARS-CoV-2 and its main morphological features¹¹. Given the ellipsoidal morphology of SARS-CoV-2, we compare both spherical and ellipsoid-shape envelopes to provide a better description of SARS-CoV-2 motion while providing the foundation for transport of another spherical-shape virus.

Spherical and ellipsoidal solids exhibit differences in their translational and rotational diffusion as the aspect ratio between the principal axis changes. For spheres, the Stokes-Einstein equation provides a direct correlation of both D_t and D_r , which is consistent with the spherical envelop model that we use herein. For ellipsoids, we validate the envelope model in terms of its average diffusivity $D_{\text{ellip}} = 1/3 \sum D_i$ (for $i = x, y, z$), with respect to the diffusivity $D_o = D|_{R=R_e}$, of an equivalent sphere with the same volume and equivalent radius R_e (see SI Sect. 4.1 for detailed description of R_e). For the SARS-CoV-2 ellipsoidal envelopes investigated, with ratios between the minor and major radius of the principal axes of 0.9 and 0.7, we obtain $D_{\text{ellip}}/D_o \sim 0.98$. This is consistent with semianalytical derivations of drag coefficients³⁸ that lead to ratios on the order of 0.99.

Surface-proteins shape. To investigate the effect of shape, we construct a model of **S** consistent with the morphologies presented in Fig. 1c. In Fig. 5, we present the reported morphology and size for the different virions investigated. Supplementary Table 10 compiles the characteristic sizes of the corresponding discretized virions in RMB. These shapes correspond to coarse representations of **S**, able to capture hydrodynamic interactions on the scale of the **S** size. Finer representations, including high-frequency sub-nanosopic details, are hindered by the overall motion of the virus, and their effect on the measured diffusivity are below the resolution of the model. Herein, the finest resolution is selected to ensure accurate hydrodynamic modelling of the different **S** morphologies.

Previous investigations have shown differences in the estimated rotational diffusion between single²⁰ and three²¹ beaded representations SARS-CoV-2 spikes. Even though three-beaded models approximate better the tetrahedral shape of the SARS-CoV-2 spikes, the minimal accurate spike representations are still to be determined.

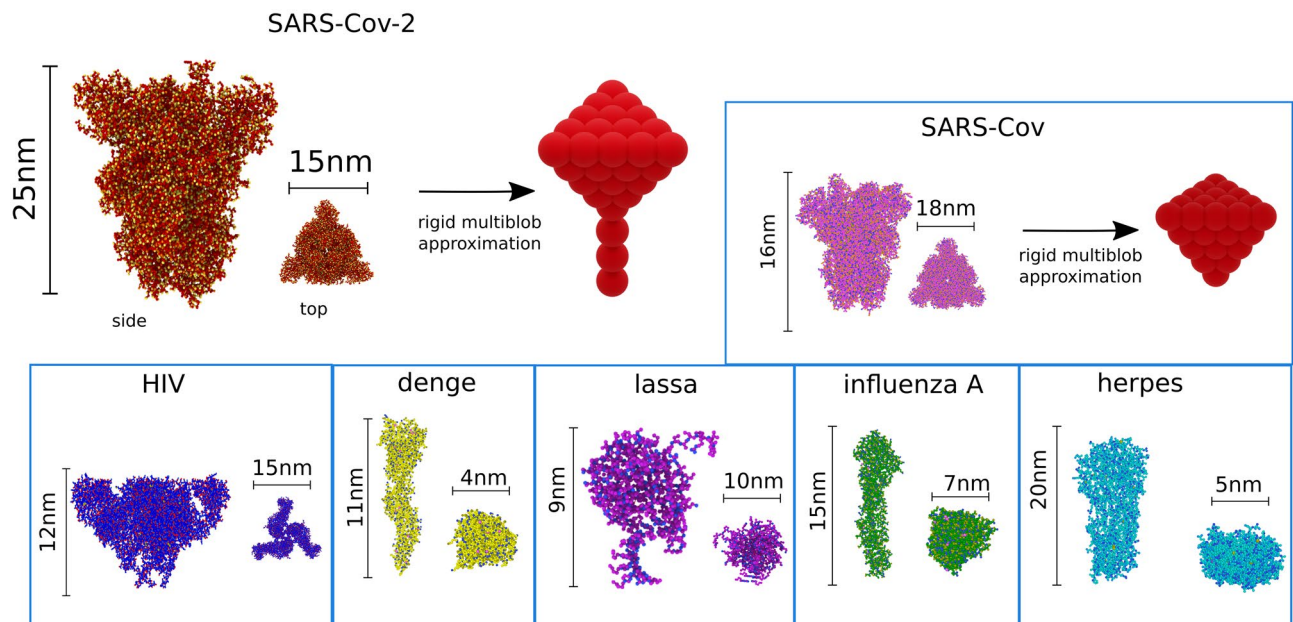


Figure 5. Discretization adopted to model the surface-protein morphology of different virions. The characteristic sizes are shown for: HIV³⁹, dengue⁴⁰, SARS-Cov-2⁴¹, SARS-Cov⁴², lassa⁴³, influenza⁴⁴, and herpes⁴⁵. The basic set of discrete morphologies are rod, tetra, sphere, rod-tetra, and rod-sphere.

To rule out effects due to discretization, we test various ratios between spike size l_s , and inter-blob distance r_o . In SI Sect. 4.3 (Supplementary Table 3) and Sect. 4.4, we present the variation on the measured diffusivity for different spike resolutions. For practical purposes, we identify that $l_s/r_o > 5$ is enough to describe within 1% error both translation and rotation of spherical objects, whereas, for tetrahedral shapes, the associated error is 8%. However, further refinement of the tetrahedral spikes allows us to reduce the error to $\sim 1\%$ (see SI Sect. 4.4, Supplementary Tables 4–5 and Supplementary Fig. 2). In Table 3 we present the computed \bar{D}_t and \bar{D}_r for SARS-CoV-2 using different resolutions. We define the error in our approximation considering the finest (most accurate and computationally expensive) resolution modelled. Table 3 includes the corresponding images of the models. Coarser representations (four blobs per S) with resolutions of $R/r_o = 3.6$ induced errors on the order of 20% for \bar{D}_r . Here, we adopt a resolution of 14.5 leading to a maximum numerical error of 0.7%.

Surface-proteins distribution. We compare the mobility of virions having homogeneously and randomly distributed S to elucidate the effects of protein sparsity. For homogeneous distributions, we localized S isotropically at equidistant positions on the surface of the envelope. For random distribution, we model ten replicas of the virion changing the position of S to obtain characteristic mean mobilities. Even though we are modelling the envelope and surface proteins as rigidly moving objects, this sampling approach is (up to a good approximation) equivalent to model virions with S that diffuses over the surface of E. In contrast, isotropically distributed proteins would correspond to S with a fixed position and consequently lower conformational freedom. We referred the reader to the SI for a detailed description of the virion construction. As a whole, we identify that virion diffusivity increases when S are localized at random positions around the surface (see Supplementary Fig. 3, Sect. 6). For all the S shapes investigated, we observe an increment on both \bar{D}_t and \bar{D}_r . The random distributions of the S induce a break in the symmetry of the virion envelope, giving, on average, enhanced mobility. Isotropically distributed S preserve the symmetry of the envelopes in a way that the hydrodynamic forces and torques originated due to the presence of S is kept balanced across the axes. As the distribution of S becomes anisotropic, this balance is broken, favouring virion mobility along some axes. At low S densities random configurations exhibit overall lower mobility reduction than homogeneous distributions. As N_s increases, the S packing become more restricted, and the symmetry-breaking effects of random distributions vanish. Owing the symmetry of spherical envelopes, the effect of S distribution appears more significant compared to the ellipsoidal ones.

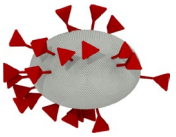
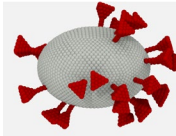
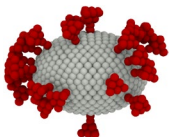
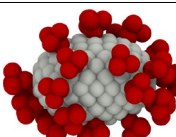
Resolution	\bar{D}_l	\bar{D}_r	R_l	R_r	Rigid model
29	0.7682	0.4162	1.133	1.171	
14.5	0.7638	0.4131	1.157	1.190	
7.2	0.7478	0.3882	1.213	1.243	
3.6	0.7075	0.3303	1.364	1.378	

Table 3. Resolution test for SARS-CoV-2 models with $N_s=26$ tetra-rod spikes. The spikes rod length is $l_s/R=0.5$ and tetrahedron width is $w_s/R=0.31$. The resolution R/r_o and computed reduced coefficients are presented. Morphology of the RMB models is included for comparison. The resolution adopted in our simulations is highlighted.

Received: 3 January 2022; Accepted: 14 June 2022

Published online: 30 June 2022

References

- Beniac, D. R., Andonov, A., Grudski, E. & Booth, T. F. Architecture of the SARS coronavirus prefusion spike. *Nat. Struct. Mol. Biol.* **13**, 751–752. <https://doi.org/10.1038/nsm1123> (2006).
- Li, S. *et al.* Acidic pH-Induced conformations and LAMP1 binding of the Lassa virus glycoprotein spike. <https://doi.org/10.1371/journal.ppat.1005418> (2016).
- Zhang, X. *et al.* Structure of acidic pH Dengue virus showing the fusogenic glycoprotein trimers. *J. Virol.* **89**, 743–750. <https://doi.org/10.1128/JVI.02411-14> (2015).
- Grünwald, K. *et al.* Three-Dimensional structure of Herpes Simplex virus from cryo-electron tomography. *Science* **302**, 1396–1398. <https://doi.org/10.1126/SCIENCE.1090284> (2003).
- Harris, A. *et al.* Influenza virus pleiomorphy characterized by cryoelectron tomography. *Proc. Natl. Acad. Sci. U.S.A.* **103**, 19123–19127. <https://doi.org/10.1073/pnas.0607614103> (2006).
- Liu, J., Bartesaghi, A., Borgnia, M. J., Sapiro, G. & Subramaniam, S. Molecular architecture of native HIV-1 gp120 trimers. *Nature* **455**, 109–113. <https://doi.org/10.1038/NATURE07159> (2008).
- Bárcena, M. *et al.* Cryo-electron tomography of mouse hepatitis virus: Insights into the structure of the coronavirus. Tech. Rep. 2 (2009).
- Zhang, J. *et al.* Structural impact on SARS-CoV-2 spike protein by D614G substitution. *Science* **372**, 525–530. <https://doi.org/10.1126/science.abf2303> (2021).
- Mansbach, R. A. *et al.* The SARS-CoV-2 spike variant D614G favors an open conformational state. *Sci. Adv.* **7**, 1–11. <https://doi.org/10.1126/sciadv.abf3671> (2021).
- Liu, C. *et al.* The architecture of inactivated SARS-CoV-2 with postfusion spikes revealed by cryo-EM and cryo-ET. *Structure* **28**, 1218–1224.e4. <https://doi.org/10.1016/j.str.2020.10.001> (2020).
- Yao, H. *et al.* Molecular architecture of the SARS-CoV-2 virus. *Cell* **183**, 730–738.e13. <https://doi.org/10.1016/j.cell.2020.09.018> (2020).
- Ke, Z. *et al.* Structures and distributions of SARS-CoV-2 spike proteins on intact virions. *Nature* **588**, 498–502. <https://doi.org/10.1038/s41586-020-2665-2> (2020).
- Neuman, B. W. *et al.* A structural analysis of M protein in coronavirus assembly and morphology. *J. Struct. Biol.* **174**, 11–22. <https://doi.org/10.1016/j.jsb.2010.11.021> (2011).
- Amitai, A., Chakraborty, A. K. & Kardar, M. The low spike density of HIV may have evolved because of the effects of T helper cell depletion on affinity maturation. *PLoS Comput. Biol.* <https://doi.org/10.1371/JOURNAL.PCBI.1006408> (2018).
- Olmsted, S. S. *et al.* Diffusion of macromolecules and virus-like particles in human cervical mucus. *Biophys. J.* **81**, 1930–1937. [https://doi.org/10.1016/S0006-3495\(01\)75844-4](https://doi.org/10.1016/S0006-3495(01)75844-4) (2001).
- Leal, J., Smyth, H. D. & Ghosh, D. Physicochemical properties of mucus and their impact on transmucosal drug delivery. *Int. J. Pharm.* **532**, 555–572. <https://doi.org/10.1016/J.IJPHARM.2017.09.018> (2017).
- Kaler, L. *et al.* Influenza A virus diffusion through mucus gel networks. *bioRxiv* 2020.08.14.251132 (2020).
- Vahey, M. D. & Fletcher, D. A. Influenza A virus surface proteins are organized to help penetrate host mucus. *eLife* **8**, 1–24. <https://doi.org/10.7554/eLife.43764> (2019).
- Murray, A. G. & Jackson, G. A. Viral dynamics: a model of the effects of size, shape, motion and abundance of single-celled planktonic organisms and other particles. *Mar. Ecol. Prog. Ser.* **89**, 103–116. <https://doi.org/10.3354/meps089103> (1992).

20. Kanso, M. A., Piette, J. H., Hanna, J. A. & Giacomini, A. J. Coronavirus rotational diffusivity. *Phys. Fluids* <https://doi.org/10.1063/5.0031875> (2020).
21. Kanso, M. A., Chaurasia, V., Fried, E. & Giacomini, A. J. Peplomer bulb shape and coronavirus rotational diffusivity. *Phys. Fluids* <https://doi.org/10.1063/5.0048626> (2021).
22. Usabiaga, F. B. *et al.* Hydrodynamics of suspensions of passive and active rigid particles: a rigid multiblob approach. *Commun. Appl. Math. Comput. Sci.* **11**, 217–296. <https://doi.org/10.2140/camcos.2016.11.217> (2016).
23. Ando, T. & Skolnick, J. Crowding and hydrodynamic interactions likely dominate in vivo macromolecular motion. *Proc. Natl. Acad. Sci.* **107**, 18457–18462 (2010).
24. Jiang, Y., Zhang, J. & Zhao, W. Effects of the inlet conditions and blood models on accurate prediction of hemodynamics in the stented coronary arteries. *AIP Adv.* **5**, 57109. <https://doi.org/10.1063/1.4919937> (2015).
25. Turoňová, B. *et al.* In situ structural analysis of SARS-CoV-2 spike reveals flexibility mediated by three hinges. *Science* **370**, 203–208. <https://doi.org/10.1126/science.abd5223> (2020).
26. Lee, N. K. *et al.* Ligand-receptor interactions in chains of colloids: when reactions are limited by rotational diffusion. *Langmuir* **24**, 1296–1307. <https://doi.org/10.1021/la701639n> (2008).
27. Cai, Y. *et al.* Structural basis for enhanced infectivity and immune evasion of SARS-CoV-2 variants. *Science* **373**, 642–648. <https://doi.org/10.1126/science.abi9745> (2021).
28. Shoup, D., Lipari, G. & Szabo, A. Diffusion-controlled bimolecular reaction rates. The effect of rotational diffusion and orientation constraints. *Biophys. J.* **36**, 697–714. [https://doi.org/10.1016/S0006-3495\(81\)84759-5](https://doi.org/10.1016/S0006-3495(81)84759-5) (1981).
29. Ozono, S. *et al.* SARS-CoV-2 D614G spike mutation increases entry efficiency with enhanced ACE2-binding affinity. *Nat. Commun.* <https://doi.org/10.1038/s41467-021-21118-2> (2021).
30. Munro, J. B. & Mothes, W. Structure and dynamics of the native hiv-1 env trimer. *J. Virol.* **89**, 5752–5757 (2015).
31. Amitai, A. Viral surface geometry shapes influenza and coronavirus spike evolution through antibody pressure. *PLoS Comput. Biol.* <https://doi.org/10.1371/journal.pcbi.1009664> (2021).
32. Liu, S. *et al.* Single-virus tracking: From imaging methodologies to virological applications. *Chem. Rev.* **3**, 1936–1979. <https://doi.org/10.1021/acs.chemrev.9b00692> (2020).
33. Coomer, C. A. *et al.* Single-cell glycolytic activity regulates membrane tension and hiv-1 fusion. *PLoS Pathog.* **16**, 1–31. <https://doi.org/10.1371/journal.ppat.1008359> (2020).
34. Aires, A., Lopez-Martinez, E. & Cortajarena, A. L. Sensors based on metal nanoclusters stabilized on designed proteins. *Biosensors* <https://doi.org/10.3390/bios8040110> (2018).
35. Hassan, A. O. *et al.* A single intranasal dose of chimpanzee adenovirus-vectored vaccine protects against sars-cov-2 infection in rhesus macaques. *Cell Rep. Med.* <https://doi.org/10.1016/j.xcrm.2021.100230> (2021).
36. Einstein, A. On the movement of small particles suspended in stationary liquids required by the molecular-kinetic theory of heat. *Ann. Phys.* **17**, 549 (1905).
37. Kim, S. & Karrila, S. J. *Microhydrodynamics: principles and selected applications* (Butterworth-Heinemann, 1991).
38. Happel, J. & Brenner, H. *Low Reynolds Number Hydrodynamics* Vol. 1 (Springer, Netherlands, 1981).
39. RCSB PDB - 3J5M: Cryo-EM structure of the BG505 SOSIP.664 HIV-1 Env trimer with 3 PGV04 Fabs.
40. RCSB PDB - 4UT6: Crystal structure of dengue 2 virus envelope glycoprotein in complex with the Fab fragment of the broadly neutralizing human antibody EDE2 B7.
41. RCSB PDB - 6ZB4: SARS CoV-2 Spike protein, Closed conformation, C1 symmetry.
42. RCSB PDB - 5XLR: Structure of SARS-CoV spike glycoprotein.
43. RCSB PDB - 4FVU: Structural basis for the dsRNA specificity of the Lassa virus NP exonuclease.
44. RCSB PDB - 6NTF: Crystal structure of a computationally optimized H5 influenza hemagglutinin.
45. RCSB PDB - 5VYL: Crystal Structure of N-terminal half of Herpes Simplex virus Type 1 UL37 protein.

Acknowledgements

This research is supported by the Basque Government through the BERC 2018-2021 programme and by the Spanish State Research Agency through BCAM Severo Ochoa excellence accreditation SEV-2017-0718 and through the project PID2020-117080RB-C55 funded by (AEI/FEDER, UE) with acronym COMPU-NANO-HYDRO. The authors acknowledge also the financial support received by the Basque Business Development Agency under ELKARTEK 2019 programme (bmG19 project: grant KK-2019/00015) and through the “Mathematical Modeling Applied to Health” Project. N.M acknowledges the support from the European Union’s Horizon 2020 under the Marie Skłodowska-Curie Individual Fellowships grant 101021893, with acronym ViBRheo. F.B.U. acknowledges support from “la Caixa” Foundation (ID 100010434), fellowship LCF/BQ/PI20/11760014, and from the European Union’s Horizon 2020 research and innovation programme under the Marie Skłodowska-Curie grant agreement No 847648.

Author contributions

N.M. and M.E. conceived the study. The first draft of the manuscript was written by N.M and D.MC, and all authors contributed to the final version of the manuscript. F.B.U developed the numerical code and methods for computing virion mobilities. D.MC conducted the simulations and data processing. All the authors discussed and analyzed the results. All authors approved the final version of the manuscript.

Competing interest

The authors declare no competing interests.

Additional information

Supplementary Information The online version contains supplementary material available at <https://doi.org/10.1038/s41598-022-14884-6>.

Correspondence and requests for materials should be addressed to N.M. or M.E.

Reprints and permissions information is available at www.nature.com/reprints.

Publisher’s note Springer Nature remains neutral with regard to jurisdictional claims in published maps and institutional affiliations.



Open Access This article is licensed under a Creative Commons Attribution 4.0 International License, which permits use, sharing, adaptation, distribution and reproduction in any medium or format, as long as you give appropriate credit to the original author(s) and the source, provide a link to the Creative Commons licence, and indicate if changes were made. The images or other third party material in this article are included in the article's Creative Commons licence, unless indicated otherwise in a credit line to the material. If material is not included in the article's Creative Commons licence and your intended use is not permitted by statutory regulation or exceeds the permitted use, you will need to obtain permission directly from the copyright holder. To view a copy of this licence, visit <http://creativecommons.org/licenses/by/4.0/>.

© The Author(s) 2022